A&A 535, A45 (2011)
DOI: 10.1051/0004-6361/201117633

Astronomy & Astrophysics

Fast inversion of Zeeman line profiles using central moments

P. Mein[1], H. Uitenbroek[2], N. Mein[1], V. Bommier[1], and M. Faurobert[3]

[1] Laboratoire d'Études Spatiales et d'Instrumentation en Astrophysique (LESIA), Observatoire de Paris, CNRS, UPMC Paris 6, Université Paris Diderot, 5 place Jules Janssen, 92195 Meudon, France
e-mail: pierre.mein@obspm.fr
[2] National Solar Observatory[4], Sacramento Peak, PO Box 62, Sunspot, NM 88349, USA
[3] UMR 6525 H. Fizeau, Université de Nice Sophia Antipolis, CNRS, Observatoire de la Côte d'Azur, Campus Valrose, 06108 Nice, France

Received 5 July 2011 / Accepted 13 September 2011

ABSTRACT

Context. Many inversion techniques derive vector magnetic fields and other parameters of the solar atmosphere from Stokes profiles with an iterative process.
Aims. We propose a new inversion method, using functions derived from central moments (ICM), to determine magnetic field vectors with very few iterations.
Methods. Two quantities A_1 and A_2 that combine moments of profiles $I \pm S$ ($S = Q, U, V$) are proposed. They are nearly linear functions of the longitudinal and transverse components of the magnetic field, and lead to estimates of the field components through a least-squares polynomial fit. A third quantity A_D can be used to interpolate between expansions that correspond to two basic models. Exponents β_1 and β_2 in the moment expressions are adjusted to minimize the sensitivity to data noise.
Results. Inversion coefficients are computed for magnetic fields up to 3000 G in the case of the 630.2 Fe I line by forward modeling in two selected 1D model atmospheres (FALC and MALTM). After inversion of synthetic profiles computed with four models at disk center (FALA, FALC, FALF, MALTM), the mean standard deviations with respect to the input fields do not exceed 5 G for both components over the full range 0–3000 G. A comparison of ICM results with inversion by the UNNOFIT code of profiles observed with THEMIS/MTR shows good agreement. The typical computing time for a solar map of 100 000 points is less than 30 s.
Conclusions. The ICM inversions are almost insensitive to thermodynamic properties and solve for vector magnetic fields in a wide range of solar conditions, ranging from plage to spot, with very little computational effort. They are, therefore, extremely suitable for large data sets. Further improvements should take into account instrumental profiles and effects of limited spatial resolution by using filling factors. Extensions using more parameters and models with large departures from the Milne Eddington approximation could also be considered.

Key words. magnetic fields – line: profiles

1. Introduction

Many inversion codes are available at present to derive magnetic field vectors from Zeeman Stokes profiles of solar lines. At the same time, these codes determine thermodynamical parameters of the solar atmosphere, which are coupled with magnetic fields in line formation. In general they employ least-squares inversion techniques, in which atmospheric parameters are modified by iterations until synthetic profiles match the observed ones (see for example the review by Bellot Rubio 2006). Some codes, SIR (Ruiz Cobo & del Toro Iniesta 1992) for example, use response functions to iteratively determine parameters at all altitudes across the atmosphere. NLTE extensions are possible (Socas-Navarro 2007). Some other codes such as UNNOFIT (Bommier et al. 2007) derive synthetic profiles with analytic expressions derived from the Milne-Eddington approximation and Unno-Rachkowsky solution (Harvey et al. 1972; Landolfi & Landi Degl'Innocenti 1982; Skumanich & Lites 1987). Multi-component atmospheres can also be investigated, with filling factors or micro-structures (MISMA code Sanchez Almeida 1997). Some other inversion codes are based on a direct comparison of observed profiles with a number of synthetic ones. They can be strongly accelerated by a principal component analysis (Rees et al. 2000; Socas-Navarro et al. 2001).

Central moments of unpolarized line profiles have been used in the past to determine velocity fields across the solar atmosphere (see for example Marmolino & Severino 1981). In the case of Zeeman sensitive lines, first order moments can be used to determine the center of gravity of the left- and right-hand circularly polarized profiles and estimate the longitudinal magnetic field (Semel 1967; Uitenbroek 2003). In this paper we expand on the use of moments, and propose the use of several quantities derived from central moments of the Stokes profiles $I \pm Q, U$ in addition to those of $I \pm V$. These quantities turn out to be nearly linear funtions of the magnetic field components along and perpendicular to the line of sight, and are mostly insensitive to other atmospheric parameters. They can be used to determine vector magnetic fields with short polynomial expansions that can be properly calibrated with forward modeling in the context of a small number of one-dimensional model atmospheres.

In Sect. 2 we define the moments that we use in Sect. 3 to find the basic quantities to be used in the inversions. In Sect. 4 we present the radiative transfer code and the four model atmospheres used to compute synthetic profiles and inversion coefficients. In Sects. 5 and 6, polynomial expansions are specified

[4] Operated by the Association of Universities for Research in Astronomy, Inc. (AURA), for the National Science Foundation.

and tested in the case of one model atmosphere. Noise effects are estimated in Sect. 7. To satisfy simultaneously a great number of solar conditions, an interpolation method is proposed and tested with different models and center-to-limb positions (Sect. 8). It is compared to UNNOFIT inversion of THEMIS/MTR data (Sect. 9). Because of the low sensitivity to thermodynamical parameters, the capabilities of a simpler method using one average model only are also investigated (Sect. 10). We end with conclusions in Sect. 11.

2. Moments of line profiles

We denote with s the Zeeman splitting corresponding to the longitudinal field $B_\parallel$, for an effective Lande factor $\overline{g}$ and a line-center wavelength λ_0:

$$s = kB_\parallel \tag{1}$$

with

$$k = 4.67 \times 10^{-14} \overline{g}\, \lambda_0^2, \tag{2}$$

where wavelengths are expressed in nm and $B_\parallel$ in Gauss. The depth of a line profile $P(\lambda)$ can be written

$$R(\lambda) = 1 - P(\lambda)/I_c, \tag{3}$$

where I_c is the continuum intensity. We note with

$$M_1(P, \beta_1) = \frac{\int_{-\infty}^{+\infty} R^{\beta_1}(\lambda)\lambda \, \mathrm{d}\lambda}{k \int_{-\infty}^{+\infty} R^{\beta_1}(\lambda) \, \mathrm{d}\lambda} \tag{4}$$

the first order moment of R, expressed in Gauss. The exponent β_1 is used to assign different weights to line wings and line center and to reduce noise effects (Sect. 8).

To characterize the widths of line profiles, we define a second moment of R similar to the classical second-order central moment:

$$M_2(P, \beta_2) = \frac{\int_{-\infty}^{+\infty} R^{\beta_2}(\lambda)\, |\lambda - \lambda_2| \, \mathrm{d}\lambda}{k \int_{-\infty}^{+\infty} R^{\beta_2}(\lambda) \, \mathrm{d}\lambda}, \tag{5}$$

where λ_2 is the wavelength corresponding to the first moment of $R(\lambda)$ to the power β_2:

$$\lambda_2 = kM_1(P, \beta_2). \tag{6}$$

We use the modulus of $\lambda - \lambda_2$ instead of $(\lambda - \lambda_2)^2$ to obtain the exact shifts of blue and red components in the case of strong transverse magnetic fields (see next section).

3. Quasi-linear functions A_1 and A_2 of magnetic field components, from weak to strong fields

For a weak line formed in a Milne-Eddington atmosphere without velocity and magnetic field, the line depth can be written as

$$R(\lambda) = c\mathrm{e}^{-(\lambda-\lambda_0)^2/d^2} \tag{7}$$

by neglecting damping effects. The coefficient c and the mean Doppler-width d depend on the line and model atmosphere.

Let us now assume a constant vector magnetic field throughout the atmosphere, and denote with $B_\parallel$ and $B_\perp$ the longitudinal and the transverse components of that field. Below we show that one can express the moments of line depths corresponding to polarized profiles $I \pm S$, $(S = Q, U, V)$ as functions of $B_\parallel$ and $B_\perp$. In this we restrict our calculations to the case of a Zeeman triplet.

3.1. $B_\parallel$ and the function A_1

Let us assume $B_\perp = 0$. As before, we denote with s the wavelength shift corresponding to the longitudinal field $B_\parallel$ and λ_0 the wavelength at line center. The line depths of $I - V$ and $I + V$ are two Gaussian functions shifted by $\pm s$ from λ_0:

$$R_{I+V}(\lambda) = c\mathrm{e}^{-(\lambda-\lambda_0-s)^2/d^2}, \tag{8}$$

$$R_{I-V}(\lambda) = c\mathrm{e}^{-(\lambda-\lambda_0+s)^2/d^2}. \tag{9}$$

The first-order moments $M_1(I+V, \beta_1)$ and $M_1(I-V, \beta_1)$ provide the centers of gravity of line depths $R_{I+V}(\lambda)$ and $R_{I-V}(\lambda)$ so that the quantity

$$A_1 \equiv \left[M_1(I + V, \beta_1) - M_1(I - V, \beta_1)\right]/2 \tag{10}$$

is equal to $B_\parallel$. This is the well-known center of gravity method for determining the line-of-sight magnetic field (Rees & Semel 1979). The result in Eq. (10) is independent of c, d and β_1.

3.2. $B_\perp$ and the function A_2

Let us assume now that $B_\parallel = 0$ and that the azimuth of $B_\perp$ is parallel to the polarization direction of Q. The line depths of $I - Q$ and $I + Q$ can be written

$$R_{I-Q}(\lambda) = c\mathrm{e}^{-(\lambda-\lambda_0-w)^2/d^2} + c\mathrm{e}^{-(\lambda-\lambda_0+w)^2/d^2} \tag{11}$$

$$R_{I+Q}(\lambda) = 2c\mathrm{e}^{-(\lambda-\lambda_0)^2/d^2}, \tag{12}$$

with

$$w = kB_\perp. \tag{13}$$

3.2.1. Weak transverse components

If the transverse component is weak ($w \ll d$), we can write

$$M_2(I - Q, \beta_2) \simeq \frac{\left(d^2 + w^2\right)}{kd\sqrt{\pi\beta_2}} \tag{14}$$

and

$$M_2(I + Q, \beta_2) \simeq \frac{d}{k\sqrt{\pi\beta_2}} \tag{15}$$

so that

$$M_2(I - Q, \beta_2) - M_2(I + Q, \beta_2) \simeq \frac{w^2}{kd\sqrt{\pi\beta_2}} \tag{16}$$

and

$$w \simeq \left(\sqrt{\pi\beta_2}\, kd\, \left[M_2(I - Q, \beta_2) - M_2(I + Q, \beta_2)\right]\right)^{1/2}. \tag{17}$$

From Eq. (15) we see that

$$d/k = \sqrt{\pi\beta_2}\, M_2(I + Q, \beta_2). \tag{18}$$

To minimize cross-talk effects between the determination of the longitudinal and transverse field components, we replace $M_2(I + Q, \beta_2)$ by the average value W of the widths of $I + V$ and $I - V$ (see Eq. (5)):

$$W = \left[M_2(I + V, \beta_2) + M_2(I - V, \beta_2)\right]/2, \tag{19}$$

so that (from Eqs. (13), (17) and (18))

$$B_\perp = \sqrt{\pi\beta_2}\, \left(W\left[M_2(I - Q, \beta_2) - M_2(I + Q, \beta_2)\right]\right)^{1/2}. \tag{20}$$

Combining Eqs. (19) and (20) we see that, for weak transverse magnetic fields,

$$A_2 \equiv [(M_2(I+V,\beta_2)+M_2(I-V,\beta_2))/2 \times (M_2(I-Q,\beta_2)-M_2(I+Q,\beta_2))]^{1/2} \quad (21)$$

is a linear function of the transverse component $B_\perp$, with a proportionality coefficient of $1/\sqrt{\pi\beta_2}$.

3.2.2. Strong transverse components

In the case of strong transverse fields ($w \gg d$)

$$M_2(I-Q,\beta_2) \simeq w/k, \quad (22)$$

so that the component $B_\perp$ is provided directly by the moment $M_2(I-Q,\beta_2)$. But at the same time $M_2(I+Q,\beta_2)$ becomes much smaller than $M_2(I-Q,\beta_2)$. We will see later that in realisitic cases (Sect. 5, Fig. 2) the width W of profiles $I+V$ and $I-V$ increases for large $B_\perp$, in such a way that A_2 remains close to a linear function of $B_\perp$ for strong fields as well as for weak fields (see Eq. (21)). It thus becomes possible to use A_2 in the full range of magnetic field strengths. In the following sections, we will express A_2 in Gauss, regardless of the (dimensionless) proportionality coefficient, which is close to $(\pi\beta_2)^{-1/2}$ for weak fields.

3.3. Magneto-optical effects

We call Φ the angle characterizing magneto-optical effects:

$$\Phi = \frac{1}{2}\arctan\left(U(\lambda_0)/Q(\lambda_0)\right), \quad (23)$$

with

$$\lambda_0 = kM_1(P,1) \quad (24)$$

$$\Phi U(\lambda_0) \le 0 \quad (25)$$

and

$$-90^0 < \Phi < 90^0, \quad (26)$$

where $U(\lambda_0)$ and $Q(\lambda_0)$ are the values of the Stokes parameters U and Q at line center of the intensity profile.

We must note that while magnetic components are related to moments integrated over full profiles, the magneto-optical effects are determined by Stokes parameters observed in one single wavelength. This leads to a higher sensitivity to noise, especially for weak transverse magnetic components, corresponding to low Q and U values. Although other more sophisticated algorithms might be investigated in this respect, we restrict the present calculations to this most simple and least time-consuming method.

4. The RH radiative transfer code

To calibrate the inversion method described here and to test its efficiency, we obtained forward solutions of the polarized radiative transfer equations with the RH radiative transfer code (Uitenbroek 2001, 2003) which is based on the Rybicki & Hummer (1991, 1992) multi-level accelerated lambda iteration scheme. The coupled equations of statistical equilibrium and radiative transfer were solved for a 23 level, 33 lines atomic model of Fe I, including the 630.25 and 630.15 nm lines. These non-LTE iterations were performed in the polarization free approximation to account for the effect of the line profile splitting on the radiative rates (Bruls & Trujillo Bueno 1996). After convergence the four Stokes parameters were calculated with the quasi parabolic DELO method developed by Trujillo Bueno (2003). In the calculation of the absorption and emission coefficients for the four Stokes parameters, the code fully accounts for the actual Zeeman splitting patterns of the atomic levels.

Four different one-dimentional hydrostatic solar atmospheric models were employed in the calculations: FALA, FALC, FALF (Fontenla et al. 1993) and MALTM (Maltby et al. 1986), representing the stratification of the quiet cell interior, averaged quiet sun, solar network and a sunspot umbra, respectively.

5. Functions A_1, A_2, W and Φ for the Fe I 630.2 nm line with the FALC model at disk center

We computed values for A_1, W , A_2 and Φ for the Fe I 630.2 nm line in the FALC model at disk center for magnetic fields in the range of $-3000 < B_\parallel < 3000$ G and $0 < B_\perp < 3000$ G, generally suitable for quiet Sun and solar active regions, with steps of 200 G for both components. The step of wavelength sampling was 2 pm after interpolation of the synthetic profiles. The exponent values in the moment computations (Eqs. (4) and (5)) are

$$\beta_1 = 1 \quad (27)$$

$$\beta_2 = 2, \quad (28)$$

according to optimizations that were chosen to minimize noise effects, as detailed in Sect. 8. Figure 1, panels (a) and (b), shows that A_1 and A_2 are nearly linear functions of $B_\parallel$ and $B_\perp$ over all ranges of considered field strengths. Magneto-optical effects are plotted in panel (c) of Fig. 1. In Fig. 2 we note the increase of W, which accounts for the almost linear asymptotic behavior of A_2 for strong transverse fields, and motivated the choice of substituting W for w in the definition of A_2. The increase in W is mainly caused by the increasing depth of the central core, because of the cross-talk of $I \pm V$ with the transverse component. Note that the obtained linearity of function A_1 with $B_\parallel$ provides clear evidence of the accuracy of the center-of-gravity determination of the line-of-sight component of the magnetic field for a large selection of longitudinal and transverse field component strentghs.

6. Polynomials $P_{1,\,\mathrm{FALC}}$, $P_{2,\,\mathrm{FALC}}$, and inversion of Fe I 630.2 nm profiles from FALC at disk center

For all synthetic profiles we have computed A_1 and A_2 after azimuth rotation over Φ, as indicated in Sect. 3.3. We first analyze the functions A_1, A_2 and Φ that were computed with the FALC model as functions of $B_\parallel$ and $B_\perp$ in the full range of useful magnetic field components.

A_1 and Φ always have the same sign as $B_\parallel$ and A_2 does not depend on the sign of $B_\parallel$. To reduce the number of coefficients, the following equations are supposed to be applied to the absolute value of A_1. If $A_1 < 0$, the final values of $B_\parallel$ and Φ must be replaced by $-B_\parallel$ and $-\Phi$.

Because A_1 is a monotonic, almost linear function of $B_\parallel$, we can expand $B_\parallel$ as a low-degree polynomial in A_1, and obtain the

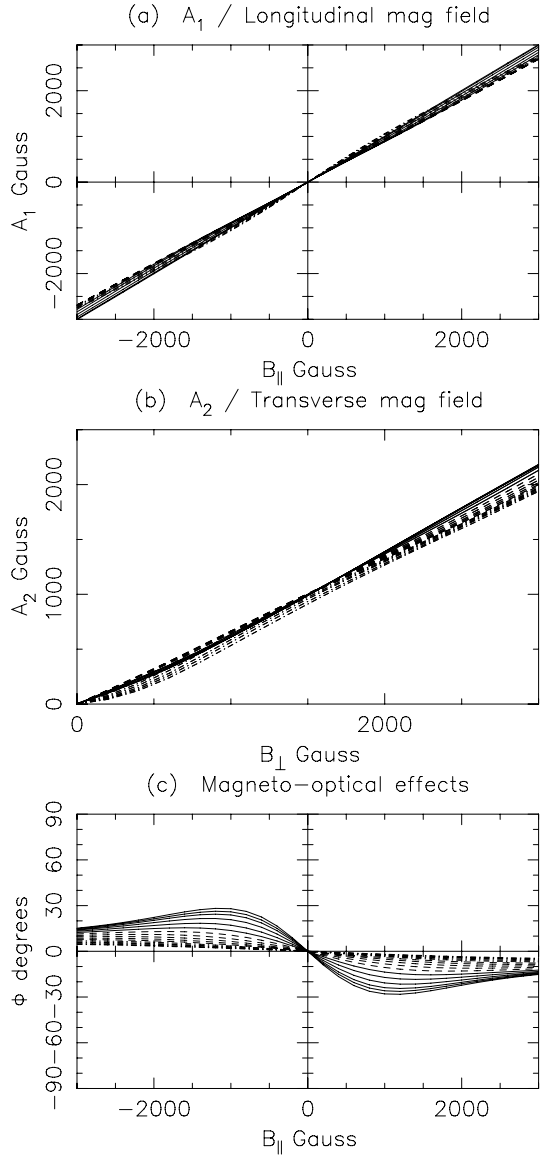

Fig. 1. Functions A_1, A_2 and Φ (Eqs. (10), (21), (23)), measured in the case of the Fe I 630.2 nm line in the FALC model at disk center. The line styles depend on the values of $B_\perp$ in panels **a)** and **c)**, and the values of $B_\parallel$ in panel **b)**: full lines until 1000 G, dashed lines until 2000 G, dashed-dotted until 3000 G.

coefficients with a least-squares fit. The coefficients depend on $B_\perp$ (see Fig. 1), so that

$$B_\parallel = \sum_m p_{1,m}(B_\perp) A_1^{m-1}. \tag{29}$$

We use polynomials with $m \leq 7$. Because the coefficients $p_{1,m}(B_\perp)$ are known for all values of $(B_\perp)$, they can also be expanded as a polynomial in $B_\perp$,

$$p_{1,m}(B_\perp) = \sum_n C_{1,m,n} B_\perp^{n-1}, \tag{30}$$

again with $n \leq 7$ and the coefficients determined by a least-squares fit from the results of the forward modeling in the FALC model. Combining both expansions, we find

$$B_\parallel = \sum_m \sum_n C_{1,m,n} A_1^{m-1} B_\perp^{n-1}. \tag{31}$$

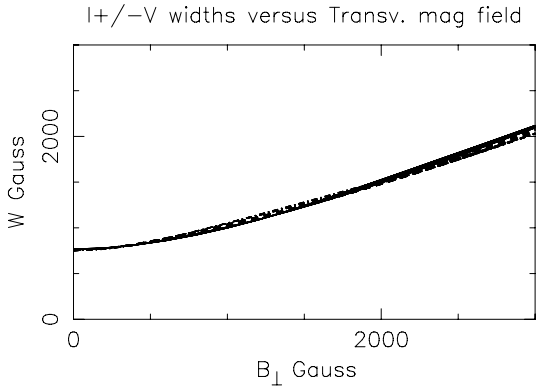

Fig. 2. Width W (Eq. (19)) in the case of the Fe I 630.2 nm line in the FALC model at disk center. Line styles are the same as in Fig. 1, panel **b)**.

In the same way, because A_2 is a monotonic function of $B_\perp$, we can determine coefficients $p_{2,m}(B_\parallel)$ so that

$$B_\perp = \sum_m p_{2,m}(B_\parallel) A_2^{m-1}, \tag{32}$$

and we can expand $p_{2,m}(B_\parallel)$ as a function of $B_\parallel$

$$p_{2,m}(B_\parallel) = \sum_n C_{2,m,n} B_\parallel^{n-1}, \tag{33}$$

so that

$$B_\perp = \sum_m \sum_n C_{2,m,n} A_2^{m-1} B_\parallel^{n-1}. \tag{34}$$

In the following, we denote with $P_{1,\mathrm{FALC}}$ and $P_{2,\mathrm{FALC}}$ the polynomials of coefficients $C_{1,m,n}$ and $C_{2,m,n}$:

$$B_\parallel = P_{1,\mathrm{FALC}}(A_1, B_\perp) \tag{35}$$
$$B_\perp = P_{2,\mathrm{FALC}}(A_2, B_\parallel). \tag{36}$$

The longitudinal and transverse field components $B_\parallel$ and $B_\perp$ can be derived from the measured quantities A_1 and A_2 by the following fast two-step iteration scheme. In the first step, $B_\parallel$ is initialized with A_1 and substituted into Eq. (36). Next the values of the two field components are derived by successive backsubstitutions:

$$X = P_{2,\mathrm{FALC}}(A_2, A_1) \tag{37}$$
$$Y = P_{1,\mathrm{FALC}}(A_1, X) \tag{38}$$
$$B_\perp = P_{2,\mathrm{FALC}}(A_2, Y) \tag{39}$$
$$B_\parallel = P_{1,\mathrm{FALC}}(A_1, B_\perp). \tag{40}$$

Magneto-optical effects can be deduced from the synthetic function Φ that we can also expand as a polynomial in $B_\parallel$ and $B_\perp$:

$$\Phi = \sum_m \sum_n C_{3,m,n} B_\parallel^{m-1} B_\perp^{n-1} \tag{41}$$
$$\Phi = P_{3,\mathrm{FALC}}(B_\parallel, B_\perp). \tag{42}$$

Because Φ is not defined for $B_\perp = 0$, extrapolated values of $P_{3,\mathrm{FALC}}(B_\parallel, 0)$ are used before computing the coefficients $C_{3,m,n}$.

To test the inversion code based on moments, we deduce vector magnetic fields from the values of A_1, A_2 calculated with the forward modeling in model FALC and the procedure outlined above in Eqs. (37) to (42). Figure 3 shows the residual errors of $B_\parallel$ and $B_\perp$ resulting from the inversion process. The standard

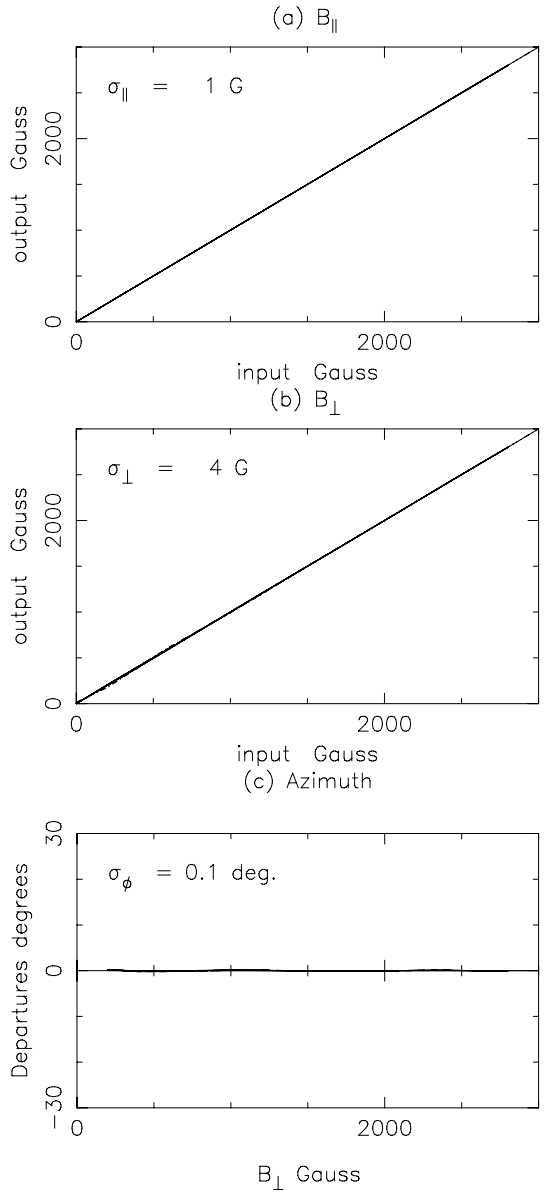

Fig. 3. Comparison of longitudinal (panel **a**)) field strength, transverse field strength (panel **b**)), and azimuth (panel **c**)) recovered with the inversion with input values.

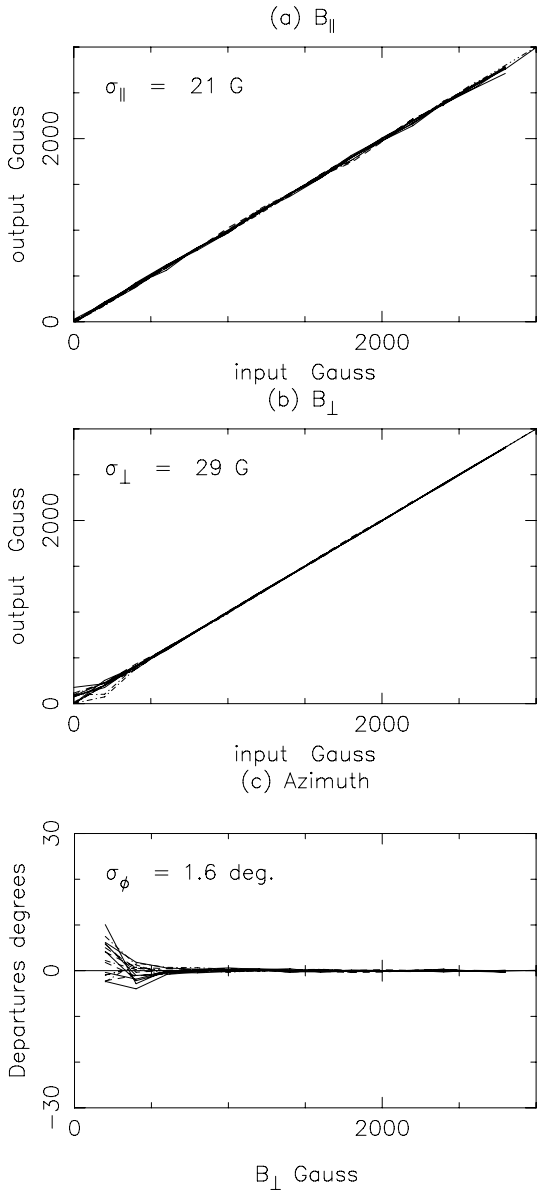

Fig. 4. Inversion of synthetic profiles for the FALC model atmosphere at disk center with noise a level of $1.5\times10^{-3} I_c$ and a sampling of 2 pm. Line styles are the same as in Fig. 1.

deviations $\sigma_{\|}$ and $\sigma_{\perp}$ are only 1 G and 4 G, respectively, over the full range of vector magnetic fields smaller than 3000 G, when least-squares polynomials are extended to 6th order. For results of the azimuth ϕ, we restrict the calculation to transverse magnetic fields larger or equal to 200 G, because the azimuth is not defined for zero fields. The standard deviation σ_{ϕ} is smaller than 1°.

7. Effects of noise

To test the effects of noise on the results, we added noise to the synthetic profiles at a level of 1.5×10^{-3} relative to the continuum intensity. This is the level assumed for typical THEMIS/MTR data (Bommier et al. 2007). This noise is simulated by a random number taken between $-3\times10^{-3} I_c$ and $3\times10^{-3} I_c$. Four different stochastic values are added to quantities I, Q, U and V.

Inversion errors are sensitive not only to the noise level, but also to the wavelength sampling of data. To mimic real observations, we used the wavelength sampling 2 pm, which is also a typical THEMIS/MTR value.

To minimize noise effects in the far line wings for moment calculations, we defined a new continuum value through the intensity at the highest and lowest wavelength in each profile. All data points with higher intensity are set to this value. In a similar way, any negative value of A_2^2 (Eq. (21)), which may appear because of noise in the case of low transverse magnetic field, is set to zero. Because of the limited number of points in the profiles, and because the results depend on the sets of stochastic numbers used to modify the synthetic data, the standard deviations are obtained by averaging over 100 successive inversions. The results which we present in Fig. 4 have standard deviations of 21 G and 29 G for both magnetic components, and 1.6° for azimuths. As expected, errors in the derived transverse component increase for very weak magnetic fields. The results are similar to the results derived from the UNNOFIT inversion of theoretical profiles (Bommier et al. 2007, their Fig. 4).

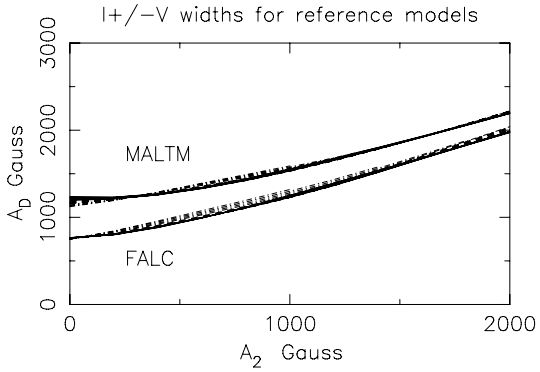

Fig. 5. Widths A_D of profiles $I \pm V$ computed with two selected models for inversion addressing several models.

8. Data from several models: interpolation using A_D functions; optimized β_1 and β_2 exponents

8.1. Definition of the function A_D

The widths of the $I + V$ and $I - V$ profiles deduced with Eq. (19) and included in the A_2 functions (Eq. (21)) vary with the different employed model atmospheres. This leads to slight variations of the coefficients in Eqs. (35) and (36), depending on which atmospheric model is used for the polynomial fits, and this leads to variations in the values of the field that are recovered by the inversions. This model dependency needs to be accounted for. So far, we used the choice exponent $\beta_2 = 2$ in Eq. (19), which was optimized to decrease the sensitivity of the inversion to noise. Setting the exponent $\beta_2 = 1$ appears to yield a quantity that is more sensitive to the model.

To deal with model dependencies more adequately, we define a new quantity A_D similar to a Doppler width:

$$A_D = [M_2(I + V, \beta_D) + M_2(I - V, \beta_D)]/2, \tag{43}$$

where we set

$$\beta_D = 1. \tag{44}$$

For each model M, $A_{D,M}$ is a monotonic function of A_2. It can be deduced from A_2 and $B_\parallel$ by an equation similar to Eq. (34):

$$A_{D,M} = \sum_m \sum_n C_{D,m,n} A_2^{m-1} B_\parallel^{n-1} \tag{45}$$

$$A_{D,M} = P_{D,M}(A_2, B_\parallel). \tag{46}$$

Figure 5 shows the A_D-functions corresponding to the two models FALC and MALTM. They look like the curves of Fig. 2 plotted for FALC with respect to $B_\perp$, except that A_2 varies roughly from 0 to 2000 G, while $B_\perp$ varies from 0 to 3000 G. Accordingly, the relevant model of any solar point can be specified by the comparison between the observed value of A_D and the value derived from Eq. (46), where $B_\parallel$ can be replaced by A_1 as a first approximation.

8.2. Inversion method

In our experiments we found that our inversion procedure yields sufficiently accurate results when we used a linear combination of polynomials P' of only two selected models: FALC and MALTM. We therefore propose an inversion procedure using linear combinations of the polynomials P_{FALC} and P_{MALTM} determined by fitting the functions A_1, A_2, Φ and A_D for these models so that

$$P_{1,\delta} = (1 - \delta)P_{1,FALC} + \delta P_{1,MALTM} \tag{47}$$

$$P_{2,\delta} = (1 - \delta)P_{2,FALC} + \delta P_{2,MALTM} \tag{48}$$

$$P_{3,\delta} = (1 - \delta)P_{3,FALC} + \delta P_{3,MALTM}, \tag{49}$$

with the fractional coefficient given by

$$\delta = \frac{A_D - P_{D,FALC}(A_2, A_1)}{P_{D,MALTM}(A_2, A_1) - P_{D,FALC}(A_2, A_1)} \tag{50}$$

according to Eq. (46), where A_1 approximates $B_\parallel$.

We show below that these linear interpolations are accurate enough because the inversion polynomials are relatively unsensitive to model parameters (Sect. 8.6).

With these modifications the inversion scheme now looks as follows:

1. determine λ_0 (Eq. (4)) and the angle Φ (Eqs. (23), (25) and (26));
2. determine new Stokes Q parameter after rotation over Φ;
3. calculate A_1, A_2, A_D and δ (Eqs. (10), (21), (46) and (50));
4. evaluate polynomials $P_{1,\delta}$ and $P_{2,\delta}$ with known coefficients and δ (Eqs. (47) and (48));
5. determine $B_\parallel$ and $B_\perp$ (Eqs. (37) to (40)), with P_δ instead of P_{FALC};
6. determine azimuth ϕ taking into account magneto-optical effects:

$$\phi = \Phi - P_{3,\delta}(B_\parallel, B_\perp), \tag{51}$$

where $P_{3,\delta}$ is deduced fromp Eq. (49).

8.3. Optimized exponents β_1 and β_2

The accuracy of inversion from data not only depends on data noise, but also on the values of β_1 and β_2. If the exponents are too small, the largest weight is assigned to the line wings, which are noise-generating, while not very sensitive to magnetic fields. On the other hand, if they are too large, only a few points of the line core are effectively involved in the moments calculations, and the effects of noise increase.

To optimize the exponents β_1 and β_2, we inverted the synthetic profiles of models FALC and MALTM, disturbed by a noise level $1.5 \times 10^{-3} I_c$, using different values of β_1 and β_2. We characterize the errors by standard deviations $\sigma_\parallel$ and $\sigma_\perp$ corresponding to the mean results from inversions in both models, for field vectors smaller than 3000 G. Figure 6 presents the standard deviations for the parallel (panel a) and perpendicular (panel b) components, respectively, as functions of the parameters β_1 and β_2 for 100 successive realizations in each case. Noise effects are roughly minimized by the choice of integer values $\beta_1 = 1$ and $\beta_2 = 2$ used in previous sections. In Fig. 6 the results corresponding to β_1 are plotted for $\beta_2 = 2$ and the results corresponding to β_2 are plotted for $\beta_1 = 1$.

8.4. Results

Table 1 presents the standard deviations between input and recovered values of magnetic field components and azimuths in the cases of synthetic profiles from models FALC, MALTM, FALA and FALF, with and without noise. In all cases the wavelegth

Table 1. Standard deviations of ICM results for magnetic components and azimuth angles with interpolations between FALC and MALTM model atmospheres using A_D functions, without and with noise.

Noise	μ	$\langle\delta\rangle$ 0	$\sigma_\parallel$ (G) 0	$\sigma_\perp$(G) 0	σ_ϕ(deg) 0	$\langle\delta\rangle$ $1.5\times10^{-3}I_c$	$\sigma_\parallel$ (G) $1.5\times10^{-3}I_c$	$\sigma_\perp$(G) $1.5\times10^{-3}I_c$	σ_ϕ(deg) $1.5\times10^{-3}I_c$
FALC	1	0.01	2	5	0	0.05	17	31	2
MALTM	1	1.01	2	4	0	0.99	16	31	1
FALA	1	0.02	2	5	0	0.06	17	31	2
FALF	1	0.03	3	5	0	0.07	18	32	2
FALC	0.75	0.03	12	8	1	0.07	24	31	2
FALC	0.50	0.02	28	15	1	0.07	39	33	2

Table 2. Standard deviations of ICM results for magnetic components and azimuth angles with average model atmosphere ($\delta = 0.5$), without and with noise.

Noise	μ	$\langle\delta\rangle$ 0	$\sigma_\parallel$ (G) 0	$\sigma_\perp$(G) 0	σ_ϕ(deg) 0	$\langle\delta\rangle$ $1.5\times10^{-3}I_c$	$\sigma_\parallel$ (G) $1.5\times10^{-3}I_c$	$\sigma_\perp$(G) $1.5\times10^{-3}I_c$	σ_ϕ(deg) $1.5\times10^{-3}I_c$
FALC	1	0.50	28	32	2	0.50	27	42	2
MALTM	1	0.50	26	34	2	0.50	37	47	2
FALA	1	0.50	25	31	2	0.50	25	41	2
FALF	1	0.50	25	29	2	0.50	25	40	2
FALC	0.75	0.50	14	23	1	0.50	20	36	2
FALC	0.50	0.50	10	17	1	0.50	27	32	2

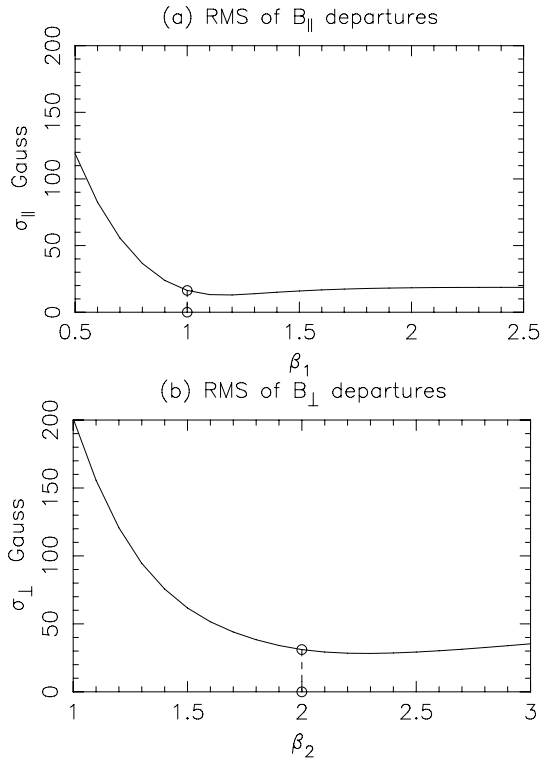

Fig. 6. Optimization of exponents β_1 and β_2 for a low sensitivity to data noise (see Sect. 8.3).

step is 2 pm. Averages are extended to all vector magnetic fields less than 3000 G, except for azimuth starting from transverse magnetic fields larger than 200 G.

Mean values $\langle\delta\rangle$ characterizing the widths of line profiles are also presented. As expected, they are close to 0 and 1 for FALC and MALTM respectively. For a given model, they increase generally with noise. The reason is probably that according to the definition of the continuum (Sect. 7), the noise decreases the mean far wing intensities and increases A_D. This increase of line widths through noise may account for the result obtained for the deviation $\sigma_\parallel$ of FALC data with $\delta = 0.05$, which is better than in the case $\delta = 0$ (Fig. 4a).

The standard deviation increases significantly with noise, showing that the errors caused by the inversion process itself can be generally neglected for real observed data.

It must be noted that the wavelength sampling used for the computation of inversion coefficients and for the inverted profiles is exactly the same as in Sect. 5. If additional interpolations are used between both sets of profiles, the σ-values without noise increase by a few Gauss, all the more because δ is also slightly affected through the A_D value. However, the results for noisy profiles are almost unchanged.

8.5. Center-to-limb effects

In Table 1 additional σ-values are given for the inversion of synthetic profiles in the FALC model corresponding to different center-to-limb positions. They are higher than values computed at disk center, but still acceptable. For any μ-value across the solar disk it is always possible to calibrate the exact coefficients of P_1 and P_2 from synthetic profiles at corresponding viewing angles and to obtain very low σ-values.

8.6. Sensitivity to model parameters

To test the sensitivity to the input models used to calibrate the expansion coefficients for the polynomials P, it is interesting to degrade the inversion code and to replace the interpolation between P_{FALC} and P_{MALTM} by the mean value $(P_{FALC} + P_{MALTM})/2$. Corresponding calculations have been performed and results similar to results of Table 1 are presented in Table 2.

For data without noise (lefthand parts of the tables), the higher accuracy of inversions with interpolations is obvious. The only exception is the last line of the tables which shows that the inversion of FALC data from $\mu = 0.5$ is more accurate with the average of P_{FALC} and P_{MALTM} from the disk center than with P_{FALC} from the disk center.

For noisy data (righthand parts) the average standard deviations $\sigma_\parallel$ and $\sigma_\perp$ for disk center increase roughly by factors 1.7

and 1.4 only from Tables 1 to 2. This means that for this noise level and this set of models, interpolations that are more sophisticated than the linear one used in Sect. 8.2 do not seem to be required.

9. Comparison with UNNOFIT inversion of THEMIS/MTR data[5]

To test our inversion code with real data, we used THEMIS/MTR observations obtained by Bommier on 2005 September 13, which were already presented in a paper dealing with azimuth ambiguity solution (Bommier et al. 2011). They concern the 630.2 Fe I line and an active region located at $L = -3.8°$ and $b = -11.7°$. Taking into account the slow variation of inversion coefficients around the disk center, as indicated in Tables 1 and 2, we can use the same disk-center polynomials as before to invert the observed profiles.

Before computing the moments for the THEMIS data, we needed to suppress the telluric blend in the red wing of the line, because we deal with ground-based data. We replaced nine points of the observed profile by a least-squares cubic interpolation. The corresponding wavelength interval is roughly 20 pm.

The exponents in the calculations of A_1, A_2 and A_D are $\beta_1 = 1$, $\beta_2 = 2$ and $\beta_D = 1$ respectively. The investigated field of view is $90'' \times 60''$.

The UNNOFIT inversion code is based on the Levenberg-Marquardt algorithm applied to the theoretical profile derived from the Unno-Rachkovsky solution of the polarized radiative transfer equation through a Milne-Eddington atmosphere (Landolfi et al. 1984) The best way to use UNNOFIT inversions is to assume inhomogeneous fields with filling factors f different from 1, and to determine the products $f * B$ (Bommier et al. 2007). But our ICM inversion does not include this model so far. Because UNNOFIT codes do exist also with $f = 1$, we made our test by comparing results obtained in that case.

The ICM computing time is very short, roughly 3×10^{-4} s per solar point with a Dell R710 computer (2.67 GHz). The results are plotted in Fig. 7. In each interval of 100 G including more than 10 points, the mean ICM values are compared to values deduced from UNNOFIT inversion (Bommier et al. 2007). Error bars of Fig. 7 correspond to standard deviations in each interval. For azimuths, the 180°-ambiguity was taken into account to compare results between −90 and +90 degrees. Intervals of 10 degrees are used in Fig. 7c, and magnetic fields smaller than 200 G are excluded as in previous sections.

Table 3 shows departures between vector magnetic field amplitudes resulting from both inversion methods in five different ranges of increasing magnetic fields. ϵ-values are mean differences and σ-values standard deviations around them. ϵ-values specify mainly systematic differences and σ-values mainly noise effects.

For weak magnetic fields, the two methods (UNNOFIT and ICM) give results that agree well, taking into account the inaccuracy resulting from the polarimetric noise.

For strong magnetic fields, the mean differences ϵ do not exceed about 50 G for vector amplitudes up to 2500 G. But the σ values are higher. They are probably partly caused by the correction of the telluric blend. Some tests have shown that the results are very sensitive to the wavelength interval used for the cubic interpolation. This might be checked by an inversion of satellite data.

In addition to blend effects, there are two other important points that have not been addressed in our ICM inversion so far:

1. instrumental profiles were not taken into account. They increase the effective width of line profiles: the computed δ-values are between 0 and 4 across the full field of view, while the expected values are between 0 (quiet regions, FALC) and 1 (spots, MALTM);
2. limitations caused by spatial resolution and seeing effects are neglected. They also increase the line widths and disturb the magnetic field determinations by mixing solar points of different B-values. A good way to eliminate part of them should be to take into account filling-factor models.

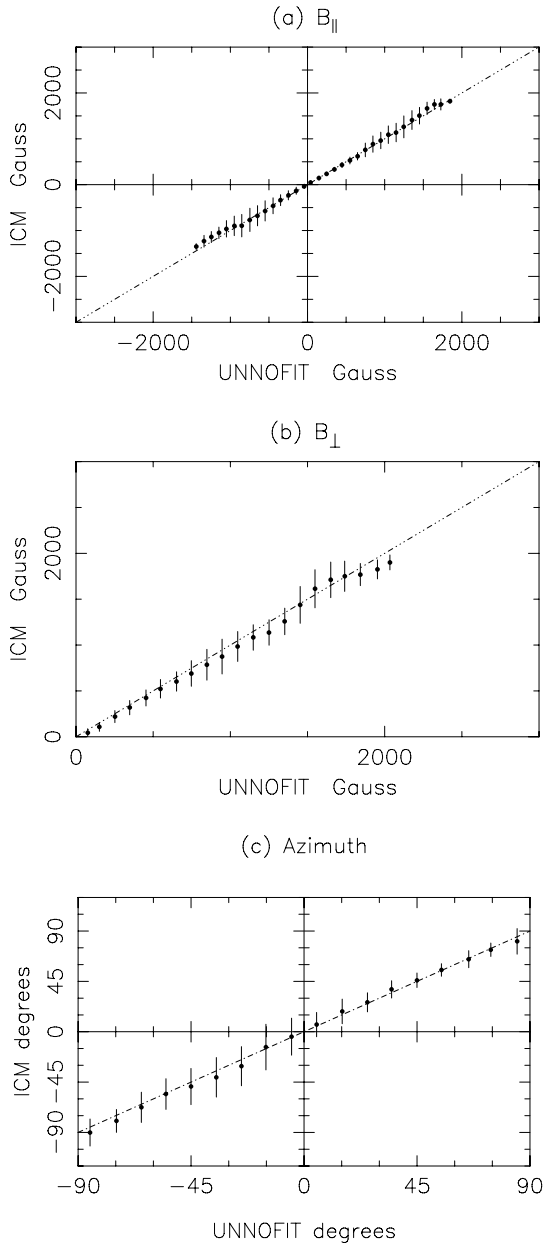

Fig. 7. THEMIS/MTR data: comparison between ICM and UNNOFIT results assuming a filling factor $f = 1$.

[5] Based on observations made with the French-Italian telescope THEMIS operated by the CNRS and CNR on the island of Tenerife in the Spanish Observatorio del Teide of the Instituto de Astrofísica de Canarias.

Table 3. Differences between ICM and UNNOFIT inversions of THEMIS/MTR data for five ranges of vector magnetic field amplitudes.

Vect. mag. field (G)	ϵ(G)	σ(G)
$0 < B < 500$	–31	43
$500 < B < 1000$	–30	107
$1000 < B < 1500$	–22	209
$1500 < B < 2000$	6	185
$2000 < B < 2500$	–51	167

Notes. ϵ = mean values, σ = standard deviations around mean values.

Table 4. Differences between ICM and UNNOFIT inversions of THEMIS/MTR data for an ICM with an average model atmosphere.

Vect. mag. field (G)	ϵ(G)	σ(G)
$0 < B < 500$	–32	42
$500 < B < 1000$	–28	101
$1000 < B < 1500$	–17	189
$1500 < B < 2000$	–2	190
$2000 < B < 2500$	–77	175

Notes. Same caption as in Table 3.

10. Shorter ICM inversion with average model atmosphere

Because of instrumental profiles and limited spatial resolution, the differences between UNNOFIT and ICM inversions of THEMIS data given in Table 3 are larger than the expected standard deviations from noise effects, even in the case of inversion by average polynomials $(P_{\rm FALC}+P_{\rm MALTM})/2$ (Sect. 8.6, Table 2).

It is interesting to compare the UNNOFIT inversion with the ICM one in the case of average polynomials. The obtained results are quite similar to the previous ones (Table 4). This suggests that before any more sophisticated way to take into account instrumental profiles and spatial resolution limitations is considered, this short ICM inversion with average coefficients may be useful to invert the observed data. The inversion scheme of Sect. 8.2 is reduced: in point 3, $A_{\rm D}$ and δ were not calculated, and point 4 is suppressed. Only three 7×7 arrays of coefficients $C_{1,m,n}$, $C_{2,m,n}$ and $C_{3,m,n}$ are necessary to perform this fast inversion for a given solar line.

11. Conclusion

Inversion methods based on central moments (ICM) determine vector magnetic fields with very few iterations in realistic model atmospheres.

They use three observable quantities, A_1, A_2 and Φ. A_1 and A_2 are nearly linear functions of magnetic field components in the full range of weak and strong fields. They are independent of mean Doppler velocities, almost independent of other thermodynmical parameters, and optimized to be also almost independent of data noise.

The extremly low number of iterations is possible because when a quantity a is a known function of two quantities b and c, and when a is a monotonic function of b, it is possible to expand b as a function of a and c:

$$a(b,c) \Longrightarrow b(a,c), \tag{52}$$

which is the case for $A_1(B_\parallel, B_\perp)$ and $A_2(B_\perp, B_\parallel)$.

The ICM inversions can simultaneously address a wide range of models by using additional quantities $A_{\rm D}$. In a shorter version, they can be used with an average model atmosphere and three fixed polynomials only.

The ICM methods are very fast (typically less than 30 s for 100 000 solar points) and very suitable for large data sets. It is possible to improve them in several ways. Instrumental profiles can be included. Solar models and an inversion process that include filling factors can also significantly increase the accuracy of the inversions. The magneto-optical effects in weak magnetic fields could be determined in more sophisticated ways that are less sensitive to noise.

We must remember that ICM methods do not require the restriction on the solution that is imposed by the Milne-Eddington inversion, namely that quantities be constant in height. Therefore, ICM methods could be very successful in determining the magnetic field structures in atmospheric conditions where the Milne-Eddington condition is not met. For example, while the ICM method presented in this paper uses the exponents $\beta_1 = 1$ and $\beta_2 = 2$, the method could be extended by varying these values, which would correspond to probing the height variation of the magnetic field, because higher β-values give more weight to the line center, which forms higher than the line wings. More generally, extended ICM inversions using more parameters may provide promising new opportunities.

Finally, we note that the present method is free of any "first guess" of the solution to initiate the iteration, contrary to most usual inversion codes that are based on the Levenberg-Marquardt algorithm for minimization.

Acknowledgements. We thank the referee for fruitful comments. Han Uitenbroek gratefully acknowledges financial support of the University of Nice Sophia Antipolis during the course of this work. This collaboration has also been supported by the CNRS through a grant of its Programme National Soleil-Terre.

References

Bellot Rubio, L. R. 2006, in ASP Conf. Ser. 358, ed. R. Casini, & B. W. Lites, 107
Bommier, V., Landi Degl'Innocenti, E., Landolfi, M., & Molodij, G. 2007, A&A, 464, 323
Bommier, V., Landi Degl'Innocenti, E., Schmieder, B., & Gelly, B. 2011, A&A, submitted
Bruls, J. H. M. J., & Trujillo Bueno, J. 1996, Sol. Phys., 164, 155
Fontenla, J. M., Avrett, E. H., & Loeser, R. 1993, ApJ, 406, 319
Harvey, J., Livingston, W., & Slaughter, C. 1972, in Line Formation in the Presence of Magnetic Fields, ed. R. Athay, L. House, & A. Newkirk (Boulder: NCAR), 227
Landolfi, M., & Landi Degl'Innocenti, E. 1982, Sol. Phys., 78, 355
Landolfi, M., Landi Degl'Innocenti, E., & Arena, P. 1984, Sol. Phys., 93, 269
Maltby, P., Avrett, E. H., Carlsson, M., et al. 1986, ApJ, 306, 284
Marmolino, C., & Severino, G. 1981, A&A, 100, 191
Rees, D. E., & Semel, M. D. 1979, A&A, 74, 1
Rees, D. E., López Ariste, A., Thatcher, J., & Semel, M. 2000, A&A, 355, 759
Ruiz Cobo, B., & del Toro Iniesta, J. C. 1992, ApJ, 398, 375
Rybicki, G. B., & Hummer, D. G. 1991, A&A, 245, 171
Rybicki, G. B., & Hummer, D. G. 1992, A&A, 262, 209
Sanchez Almeida, J. 1997, ApJ, 491, 993
Semel, M. D. 1967, Annales d'Astrophysique, 30, 513
Skumanich, A., & Lites, B. W. 1987, ApJ, 322, 473
Socas-Navarro, H. 2007, ApJS, 169, 439
Socas-Navarro, H., López Ariste, A., & Lites, B. W. 2001, ApJ, 553, 949
Trujillo Bueno, J. 2003, in Stellar Atmosphere Modeling, ed. I. Hubeny, D. Mihalas, & K. Werner (San Francisco, CA: ASP), ASP Conf. Ser., 288, 582
Uitenbroek, H. 2001, ApJ, 557, 389
Uitenbroek, H. 2003, ApJ, 592, 1225